The significance of dose heterogeneity on the anti-tumor response of minibeam radiation therapy

Sarah Potiron, Lorea Iturri, Marjorie Juchaux, Julie Espenon, Cristèle Gilbert, Josie Mcgarrigle, Ramon Ortiz Catalan, Alfredo Fernandez-Rodriguez, Catherine Sebrié, Laurène Jourdain, et al.

Radiotherapy and Oncology 201 (2024) 110577

Contents lists available at ScienceDirect

Radiotherapy and Oncology

journal homepage: www.thegreenjournal.com

Original Article

The significance of dose heterogeneity on the anti-tumor response of minibeam radiation therapy

Sarah Potiron [a,b,1], Lorea Iturri [a,b,1], Marjorie Juchaux [a,b], Julie Espenon [a,b], Cristèle Gilbert [a,b], Josie McGarrigle [c], Ramon Ortiz Catalan [a,b], Alfredo Fernandez-Rodriguez [a,b], Catherine Sebrié [d], Laurène Jourdain [d], Ludovic De Marzi [e,f], Gilles Créhange [e,f], Yolanda Prezado [a,b,*]

[a] Institut Curie, Université PSL, CNRS UMR3347, Inserm U1021, Signalisation Radiobiologie et Cancer, 91400 Orsay, France
[b] Université Paris-Saclay, CNRS UMR3347, Inserm U1021, Signalisation Radiobiologie et Cancer, 91400 Orsay, France
[c] Imperial College London, Exhibition Road, London SW7 2AZ, United Kingdom
[d] Service Hospitalier Frederic Joliot, CEA, CNRS, Inserm, BIOMAPS Universite Paris-Saclay, Orsay, France
[e] Institut Curie, Université PSL, Université Paris-Saclay, Inserm U1288, Laboratoire d'Imagerie Translationnelle en Oncologie (LITO), 91898 Orsay, France
[f] Institut Curie, Radiation Oncology Department, PSL Research University, 25 rue d'Ulm 75005, Paris/Orsay, France

A B S T R A C T

Background and purpose: Proton Minibeam Radiation Therapy (pMBRT) is an unconventional radiation technique based on a strong modulation of the dose deposition. Due to its specific pattern, pMBRT involves several dosimetry (peak and valley doses, peak-to-valley dose ratio (PVDR)) and geometrical parameters (beam width, spacing) that can influence the biological response. This study aims at contributing to the efforts to deepen the comprehension of how the various parameters relate to central biological mechanisms, particularly anti-tumor immunity, and how these correlations affect treatment outcomes with the goal to fully unleash the potential of pMBRT. We also evaluated the effects of X-ray MBRT to further elucidate the influence of peak dose and dose heterogeneity.
Methods and Materials: An orthotopic rat model of glioblastoma underwent several pMBRT configurations. The impact of different dosimetric parameters on survival and on the modulation of crucial mechanisms for pMBRT, such as immune response, was investigated. The latter was assessed by immunohistochemistry and flow cytometry at 7 days post-irradiation.
Results: Survival was improved across the various pMBRT regimens via maintaining a minimum valley dose as well as a higher dose heterogeneity, which is driven by peak dose. While the mean dose did not impact immune infiltration, a higher PVDR promoted a less immunosuppressive microenvironment.
Conclusions: Our results suggest that both tumor eradication, and immune infiltration are associated with higher dose heterogeneity. Higher dose heterogeneity was achieved by optimizing the peak dose, as well as maintaining a minimum valley dose. These parameters contributed to direct tumor eradication as well as reduction of immunosuppression, which is a departure from the more immunosuppressive tumor environment found in conventional proton therapy that delivers uniform dose distributions.

Introduction

Proton minibeam radiation therapy (pMBRT) [1,2] is a type of spatially fractionated radiation therapy (SFRT), that uses submillimetric beams, resulting in dose distributions composed of regions depositing high doses (peaks) and regions depositing low doses in between (valleys). pMBRT offers great promise for an efficient treatment of intractable tumors, such as glioblastomas [3–6], while remarkably reducing normal tissue toxicities in preclinical studies [7–10]. The dose distributions consist of areas of high doses (peaks) and low doses (valleys). Successful veterinary trials on dogs with spontaneous gliomas encourage future clinical trials in humans [11].

pMBRT appears to activate distinct radiobiological mechanisms [12]. The literature in SFRT points at several mechanisms of action, including differential vascular effects [13–16], cell signaling effects [17,18], stem cell migration [19], free radical production and diffusion covering the valley regions in the tumors [20], inflammation and immunomodulatory effects [21–24] including abscopal effects at the tumor and healthy tissue level [25]. Recent work highlights the crucial role of T cells in the anti-tumor response of X-ray MBRT [24] and the establishment of long-term antitumor immunity [24].

The multiparametric and multiscale nature of SFRT presents new

* Corresponding author at: Institut Curie, Université PSL, CNRS UMR3347, Inserm U1021, Signalisation Radiobiologie et Cancer, 91400 Orsay, France.
E-mail addresses: sarah.potiron@curie.fr (S. Potiron), lorea.iturri@curie.fr (L. Iturri), yolanda.prezado@curie.fr (Y. Prezado).
[1] Contributed equally.

https://doi.org/10.1016/j.radonc.2024.110577
Received 13 May 2024; Received in revised form 24 September 2024; Accepted 3 October 2024
Available online 10 October 2024

challenges for dose prescription and treatment planning. Unlike conventional RT, pMBRT requires consideration of multiple parameters, including peak dose, valley dose, beam width, spacing and peak-to-valley dose ratio (PVDR), each potentially influencing treatment outcomes (i.e. tumor control and normal tissue sparing). However, the correlations between these parameters and the biological response are not yet completely understood [26]. A retrospective evaluation highlighted valley dose as a key parameter in SFRT correlating with increased lifespan (ILS) in tumor-bearing rodents, whereas peak dose, commonly used for dose prescription in SFRT [27], showed a weaker correlation [26].

The main goal of this work was to expand on those initial evaluations. With this aim, the correlation between key dosimetric parameters (peak and valley doses, PVDR) with treatment outcomes (ILS, proportion of long-term survivals free of tumor, and immune infiltration) was assessed. To the best of our knowledge, this is the first evaluation of this kind in pMBRT. These findings will provide insights into the optimization of key dosimetric parameters in pMBRT, guiding preclinical research for better tumor control and reduced toxicities, and the translation into clinical trials for the treatment of challenging tumors.

Materials and Methods

Ethics statement: All animal experiments were conducted in accordance with the animal welfare and ethical guidelines of our institution. They were approved by the French Ministry of Research (permit n° 2,019,122,418,442,057 and 2022040609163783). Animals were housed at the Institut Curie animal facility accredited by the French Ministry of Agriculture for performing experiments on rodents.

Tumor inoculation and follow-up

The RG2-[D74] (ATCC® CRL-2433™, RRID: CVCL_3581) glioma cell line [28], transfected with the luciferase gene, was used. $5x10^5$ RG2-Luc cells were suspended in 5 μL of DMEM, then injected intracranially into 6-week-old male immunocompetent rats (Fischer 344, Janvier Labs and Charles River, France) using a Hamilton syringe through a burr hole in the right caudate nucleus (coordinates relatives to Bregma: Anterior-Posterior: −1 mm; Median-Lateral: +4 mm; Dorsal-Ventral: −5.5 mm from the skull).

The presence of a tumor was confirmed by Bioluminescence Imaging (BLI) or in the case of the survival analysis study by both BLI and Magnetic Resonance Imaging (MRI) before irradiation. Details on the methodology can be found in Supplemental materials.

Irradiation and dosimetry

All the irradiations were performed at the pencil beam scanning (PBS) beamline of Orsay Proton Therapy Center 14 days after tumor inoculation. The proton energy at the isocenter was 100 MeV. A 65-mm-thick divergent brass multislit collimator was attached to the nozzle exit to shape the planar minibeams [29]. Dosimetry was performed following the methodology described in a previous paper [30]. Radiochromic films were then placed on the skin for quality assurance of the irradiation.

For all studies, irradiations were performed at a conventional PBS dose-rate of 4 ± 0.02 Gy/s. In a first study (Study 1, Table 1), two different pMBRT collimators (20 mm × 400 ± 50 μm slits), differing in their center-to-center (c-t-c) distances (2.0 mm and 2.8 mm) were employed. The animals were irradiated at the plateau of the Bragg curve to maintain the same valley (10 Gy) and similar average doses (around 23 Gy, therapeutic dose [4]), with a different level of dose heterogeneity quantified by the so called peak-to-valley dose ratio (PVDR, i.e. the ratio between peak and valley doses).

Since valley dose appears to dominate the correlation between dosimetric parameters and ILS [26], it was relevant to make a comparison in terms on immune infiltration between pMBRT and conventional proton therapy (CPT, uniform dose deposition) in terms of similar valley dose (Study 2, Table 1).

Graphical representations and dose distribution maps of each proton beam therapy configurations are described in Fig. S1**A-B**.

Finally, to decorrelate the influence of the peak dose and PVDR a dose escalation study was carried out (Study 3, Table 1) using the SARRP (Small Animal Radiation Research Platform). In this case, the dose heterogeneity (PVDR) is maintained constant with the use of a unique collimator (c-t-c distance = 1.4 mm), with valley doses only slightly contrasting the peak doses, which ranged from 27 to 84 Gy. This study was performed at a small animal irradiator using X-ray MBRT [29], as the equipment is more accessible than the clinical proton beamline.

The rats received isoflurane at a concentration of 2.5 % under a mixture of medical air and oxygen supplementation when being irradiated.

Animal follow-up

Glioblastoma-bearing rats were irradiated 14 days after the tumor inoculation and euthanized 7 days after radiation treatment for flow cytometry (FACS) and immunohistochemistry (IHC) analysis, since this timepoint is corresponding to the peak of infiltration in our model [24]. Long-term survival analysis was conducted for 3 months after irradiation. MRI acquisitions were performed at 24 h before irradiation, at 5 days, 16 days and 3 months post-irradiation, and tumor volume measured.

The clinical status was checked five times per week. Any rat showing classical adverse neurological signs related to tumor growth (i.e., substantial weight loss, > 10 % of weight within 24 h) was humanely euthanized using CO_2 asphyxia.

Table 1
Distribution of the experimental groups used in this study. Doses are given at the tumor implantation depth.

						Number of animals		
	Configuration	c-t-c distance	Peak dose (Gy)	Valley dose (Gy)	Average dose (Gy)	Survival	Flow cytometry	IHC
Study 1 (Figs. 1-2)	pMBRT 2.8 mm	2.8 mm	49.5 ± 2.4	10 ± 0.5	23 ± 1.0	9	8	6
	pMBRT 2.0 mm	2.0 mm	31 ± 2.0	10 ± 0.5	21.5 ± 1.0	9	7	5
	Non-irradiated	N/A	N/A	N/A	N/A	7	6	12
Study 2 (Fig. 3)	pMBRT 2.8 mm	2.8 mm	49.5 ± 2.4	10 ± 0.5	23 ± 1.0	N/A	8	N/A
	CPT 10 Gy	N/A	N/A	N/A	10 ± 0.5	N/A	8	N/A
	Non-irradiated	N/A	N/A	N/A	N/A	N/A	7	N/A
Study 3 (Fig. 4)	MBRT 10 Gy	1.4 mm	27.7 ± 1.4	1.5 ± 0.1	10	N/A	8	N/A
	MBRT 15 Gy	1.4 mm	42 ± 2	2.2 ± 0.1	15	N/A	8	N/A
	MBRT 20 Gy	1.4 mm	55 ± 3	3.0 ± 0.2	20	N/A	8	N/A
	MBRT 30 Gy	1.4 mm	84 ± 4	4.5 ± 0.2	30	N/A	5	N/A
	Non-irradiated	N/A	N/A	N/A	N/A	N/A	6	N/A

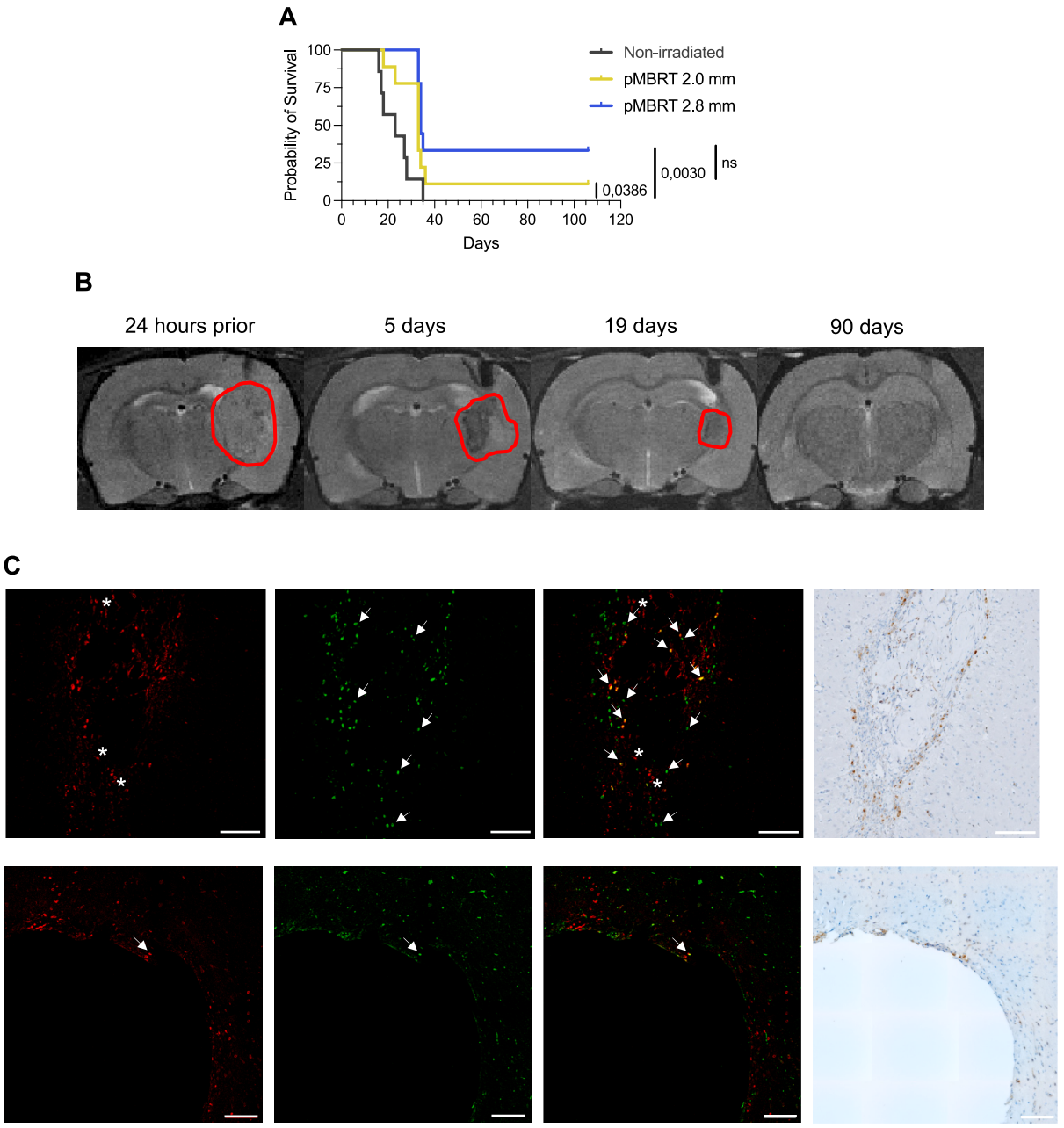

Fig. 1. Peak and valley doses influence survival rate in glioblastoma. (A) Survival curves of the non-irradiated controls (black line, n = 7), pMBRT c-t-c of 2.0 mm (yellow line, n = 9) and pMBRT c-t-c of 2.8 mm (blue line, n = 9). The differences were significant for the log-rank (Mantel-Cox) test. (B) Representative longitudinal MRI monitoring of a survivor 3-months after pMBRT 2.8 mm treatment. (C) Immunohistochemistry staining of immune cells 3 months after irradiation on long-term survivors. Upper panel shows the pre-existing tumor bed in one of the long-term survivors in the pMBRT 2.8 mm group. Lower panel shows the scar in a representative long-term survivor belonging to the pMBRT 2.8 mm group. Right arrows point at examples of $CD3^+$ $CD8^{neg}$ T cells (only green), left arrows point at $CD3^+$ $CD8^+$ T cells examples (coexpression, yellow) and asterisks mark examples of $CD3^{neg}$ $CD8^+$ macrophages (only red). Scale bar: 100 µm. (For interpretation of the references to colour in this figure legend, the reader is referred to the web version of this article.)

Analysis of tumor and brain immune cell populations

Tumors were harvested from the rat and weighed and immediately processed enzymatically and mechanically by incubation in digestive solution containing Dulbecco's Phosphate Buffered Saline (D-PBS, Gibco), 1 mg/mL Collagenase D (Roche), 0.1 mg/mL DNAse I (Sigma-Aldrich) and 3 % fetal calf serum (FCS)) for 40 min at 37 °C in a tissue dissociator (gentleMACS, Miltenyi Biotec). The resulting single cell suspension was resuspended in FACS buffer (D-PBS with 0.5 % bovine serum albumin (BSA) and 2 mM ethylene-diamine-tetra-acetic acid (EDTA)) and filtered and centrifuged. Samples were resuspended in Debris Removal Solution (Miltenyi Biotec) following manufacturer's instructions. Cells were blocked with purified anti-CD32 (FcγRII) as a blocking agent. Incubation of cells was done in a viability stain and immunolabelled in buffer containing PBS and 3 % FCS (Table S1). Counting beads were added to the sample before acquisition (Count-Bright™ Plus Absolute Counting Beads, Thermofisher).

Cell profiles were recorded using a multiparameter flow cytometer (Fortessa LSR, BD Bioscience) and analyzed using FlowJo™ v10.6 software (BD Life Sciences).

Histopathology and multiplexed immunofluorescence

During rat necropsy, the brains were carefully removed and fixed in zinc formalin fixative for histopathologic and multiplex immunofluorescence (IF) analysis. The brains were embedded in paraffin wax and then trimmed in serial 5-µm-thick coronal sections.

Multiplexed IF staining was performed on brain sections of long-term survivors as well as on rats euthanized 7 days after treatment, to identify the presence of immune cells along blood vessels.

CD3 and CD8 antibodies were used to target immune cells and the need for signal amplification was overcome with fluorochrome-coupled secondary antibodies (**Table S2**). Sections were mounted with Fluoroshield (Sigma-Aldrich).

Vascular endothelial cells were labelled with CD31 and detected using a biotinylated horse Goat anti-Rabbit secondary antibody (**Table S3**). More details can be found in Supplemental materials.

To investigate a potential co-localization of immune and vascular endothelial cells, serial cuts were labelled for CD31 and for CD3 and CD8 and their corresponding fluorochrome-coupled secondary antibodies for amplification as previously reported.

Imaging and data quantification

Confocal imaging was performed using a Leica SP5 FLIM microscope equipped with a DM10006 inverted microscope stand. The mapping acquisition of the tumor volume at 7 days post pMBRT treatment was performed using an AxioZoom Apotome 2 motorized (Zeiss) equipped with an advanced XCite fluorescence illumination system. Finally, AxioImager M2 microscope was used to visualize transmitted light imaging, specifically for hematoxylin and eosin (H&E) and CD31 staining (**Table S3**).

Quantitative data were obtained using Fiji (version 2.14.0/1.54f) and the MIC-MAQ plugin (version 1.03) [31]. Details about the methodology can be found in Supplemental materials.

Statistical analysis

Statistical analysis was performed by Brown-Forsythe and Welch ANOVA with multiple comparisons performed by Unpaired t with Welch's correction. These statistical analyses were performed on GraphPad Prism 10 (GraphPad Software, CA, United States). The log-rank (Mantel-Cox) test was used to analyze the survival data. Data resulting from flow cytometry of immune cell populations in tumor samples is expressed as mean ± standard error of the mean.

Results

This section reports the results obtained regarding the influence of the peak, valley doses, and their ratio on the survival time, tumor eradication and immune infiltration into the tumor microenvironment (TME).

Fig. 1**A** shows the survival curves of Study 1 (Table 1). The median overall survival time was significantly higher in the two irradiated groups compared to the non-irradiated animals. No statistically significant difference was observed between the irradiated groups (Fig. 1**A**). However, the pMBRT treatment employing a collimator with a 2.8 mm c-t-c distance, and thus, a higher peak dose and dose heretogeneity (PVDR = 5), yielded a higher number of long-term survivors free of tumors (3 out of 9) compared to the other configuration (1 out of 9; PVDR = 3). Correspondingly, MRI follow-up revealed a tumor regression to a non-visible state 3 months after treatment in the long-term survivals, as demonstrated in a representative long-term survivor in the pMBRT 2.8 mm c-t-c treated group (Fig. 1**B**).

$CD3^+$ and $CD8^+$ T cells and $CD8^+$ macrophages were present in the pre-existing tumor bed in the long-term survivals of the group irradiated with the 2.8 mm c-t-c distance, suggesting immune surveillance 3 months after treatment. Notably, in one of the survivors, a small yet highly vascularized area was discerned. Within this area, T cells and macrophages were closely positioned near the tumor bed (Fig. 1**C**). No visible scar was found in the survivor from the 2.0 mm c-t-c group.

A significant alteration in the immune cell composition of the tumors after pMBRT irradiation, in particular T lymphocytes (expressing CD3, including CD4 and CD8 populations) (Fig. 2**A-C, gating strategy in Fig. S2**) was observed, with no significance between both irradiated groups. Interestingly, the cell density of regulatory T cells (Tregs, identified as $CD4^+$ $CD25^+$ T cells) was increased in the pMBRT 2.0 mm c-t-c group (7 animals) with respect to non-treated animals (6 animals) and to pMBRT 2.8 mm c-t-c group (8 animals, Fig. 2**D**). The density of tissue resident memory T cells (TRM T cells, characterized as $CD8^+$ $CD103^+$ T cells) was similar between the irradiated groups with a significant difference with respect to non-irradiated group (Fig. 2**E**). These results indicate the establishment of an adaptative immune response within the TME, along with an antigen memory formation.

Additionally, the cell density of other key players in immune response, such as natural killer (NK) cells (identified as $CD3^{neg}$ $CD161^{high}$ $CD8^+$) and B cells (characterized as $CD3^{neg}$ $B220^{high}$ $Rt1b^+$), displayed a non statistically significant trend towards a higher value in the irradiated groups as compared to the control group (Fig. 2**F-G**). Moreover, pMBRT 2.0 mm c-t-c treatment induced a significant increase in neutrophils (identified as $CD11b/c^+$ $His48^+$ $CD43^{dim}$) (Fig. 2**K**).

The multiplexed IF analysis was conducted on the whole tumor section (**Fig. S5**). A substantial tumor infiltration of immune cells is observed in all groups, in agreement with the FACS analyses (**Fig. S6**). A significant elevation of $CD8^{neg}$ T cells and $CD8^+$ T cells (Fig. 2**N and 2O** respectively) after pMBRT 2.8 mm c-t-c treatment was observed, while $CD8^+$ macrophages exhibited a reduction following pMBRT irradiations (Fig. 2**P**).

Overall, these findings indicate an activation of the immune response against the tumor following both pMBRT configurations, with a trend to be more immunosuppressive in the 2.0 mm c-t-c (more homogenous dose distribution) case.

A notable shift in the immune cells composition in the TME after both radiation treatments (Fig. 3) was observed with a significantly increased infiltration of T cells in both irradiation patterns (8 animals for each configurations were used) with respect to the non-irradiated group (7 animals, Fig. 3**A-C**). pMBRT displayed a non-statistically significant trend toward higher density of Tregs compared to CPT and non-irradiated groups (Fig. 3**D**), The increase in TRM T cells was similar for both pMBRT and CPT treatments, indicating the same establishment of an antigen memory (Fig. 3**E**). Only the CPT irradiated rats displayed a statistical difference concerning NK cells, with respect to pMBRT and control groups (Fig. 3**F-G**). Interestingly, $CD43^+$ monocytes, neutrophils and $CD49d^{neg}$ macrophages were highly increased after CPT treatment, indicating a more immunosuppressive cell recruitment composed of a combination of cell types, with regards to the pMBRT and control groups (Fig. 3**J-K,M**).

In this evaluation, the dose heterogeneity was kept constant, and a dose escalation was performed using X-ray MBRT (Table 1). Lymphocytes were specifically examined due to their role in the antitumor response after MBRT [24]. Once again, a remarkable infiltration of T cells was observed after all MBRT doses in all subpopulations analyzed (Fig. 4**A-E**). Globally there are not statistically significant differences in terms of T cells infiltration among the irradiated groups, and that independently of the peak and valley doses employed.

Discussion

pMBRT has already exhibited a remarkable widening of the therapeutic window for highly radioresistant tumors in preclinical models [2,3,6]. The use of protons comes with several advantages with respect to X-rays: i) the multiple coulomb scattering of the protons increases the valley dose as a function of depth, so it is feasible to achieve high enough

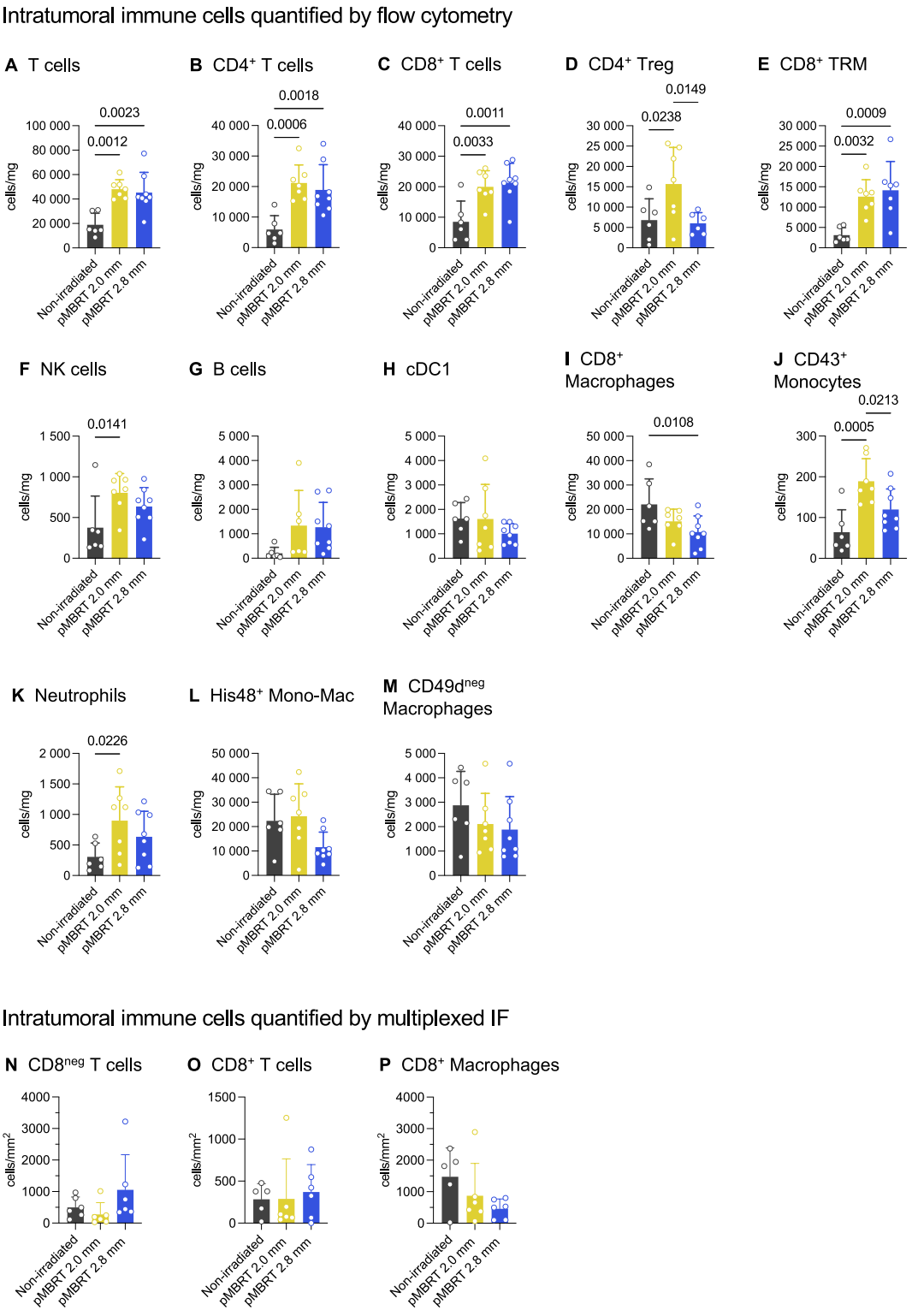

Fig. 2. Peak and valley dose also influence the immune infiltration in glioblastoma. FACS analysis of immune cells in glioblastoma 7 days after irradiation. (A) Cell density as recovered cells per milligram of tissue including all T cells, (B) $CD4^+$ T cells, (C) $CD8^+$ T cells, (D) regulatory T cells ($CD4^+$ Tregs), (E) tissue resident memory ($CD8^+$ TRM) T cells, (F) B cells, (G) natural killer (NK) cells, (H) conventional dendritic cells type 1 (cDC1), (I) neutrophils, (J) $CD8^+$ macrophages, (K) $CD43^+$ $His48^{neg}$ monocytes, (L) $His48^+$ $CD43^{neg}$ monocytes-macrophages (mono-mac), (M) $CD49d^{neg}$ macrophages. The data are presented as the mean ± standard deviation (SD). The differences were significant for the log-rank (Mantel–Cox) test (Chi square = 52.42, df = 4, $p < 0.0001$). Multiplexed immunofluorescence analysis of immune cells in glioblastoma 7 days after irradiation. (N) Quantification of $CD8^+$ tumor T cells ($CD3^+$ $CD8^{neg}$) density expressed in cells/mm^2 of tissue, (O) $CD3^+$ $CD8^+$ T cells, and (P) $CD8^+$ Macrophages.

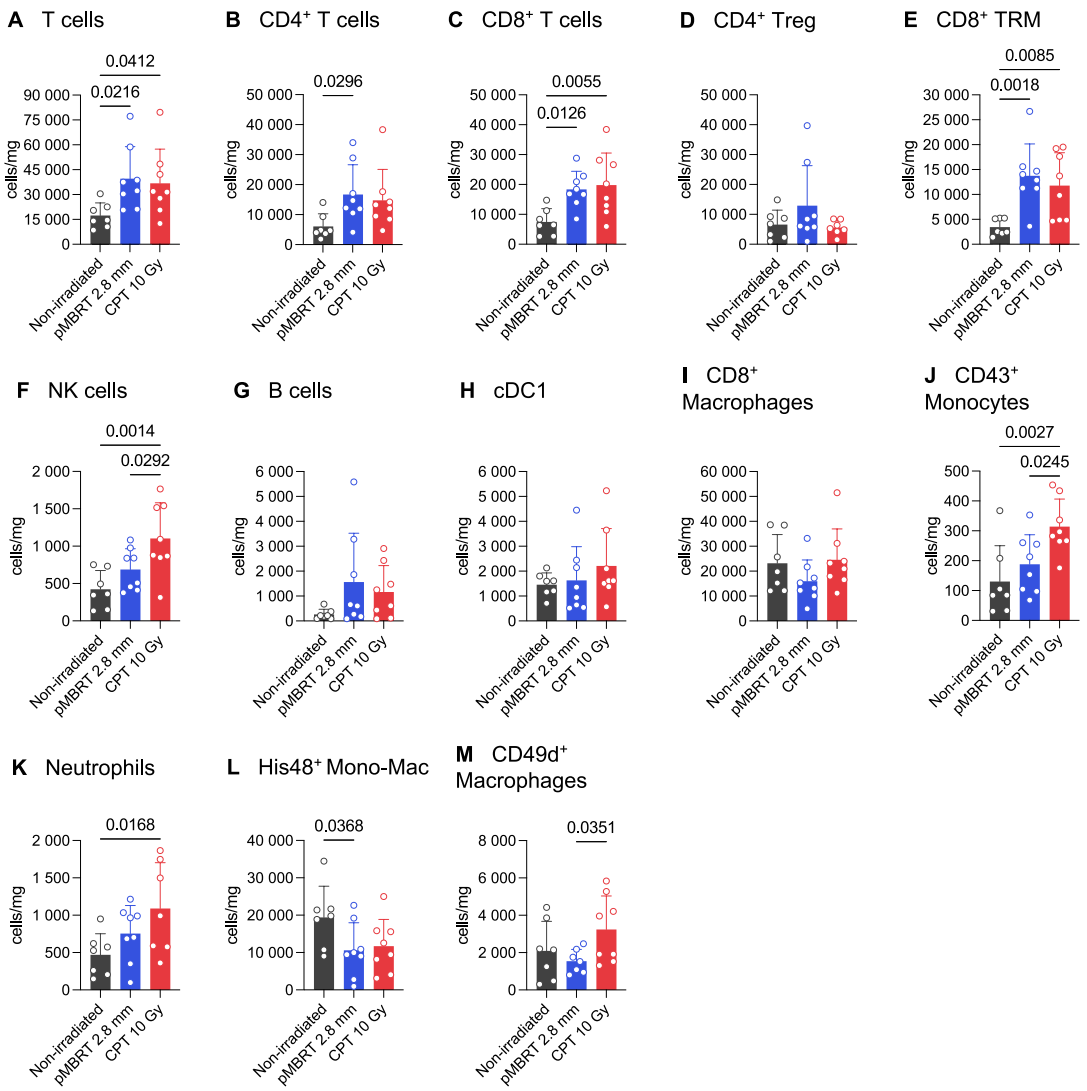

Fig. 3. Similar immune infiltration in valley dose-equalling homogeneous radiation dose. FACS analysis of immune cells in glioblastoma 7 days after irradiation. (A) Cell density including all T cells, (B) $CD4^+$ T cells, (C) $CD8^+$ T cells, (D) regulatory T cells ($CD4^+$ Tregs), (E) tissue resident memory ($CD8^+$ TRM) T cells, (F) B cells, (G) natural killer (NK) cells, (H) $CD8^+$ macrophages, (I) neutrophils, (J) conventional dendritic cells type 1 (cDC1), (K) $His48^+$ $CD43^{neg}$ monocytes-macrophages (mono-mac), (L) $CD43^+$ $His48^{neg}$ monocytes, (M) $CD49d^{neg}$ macrophages.

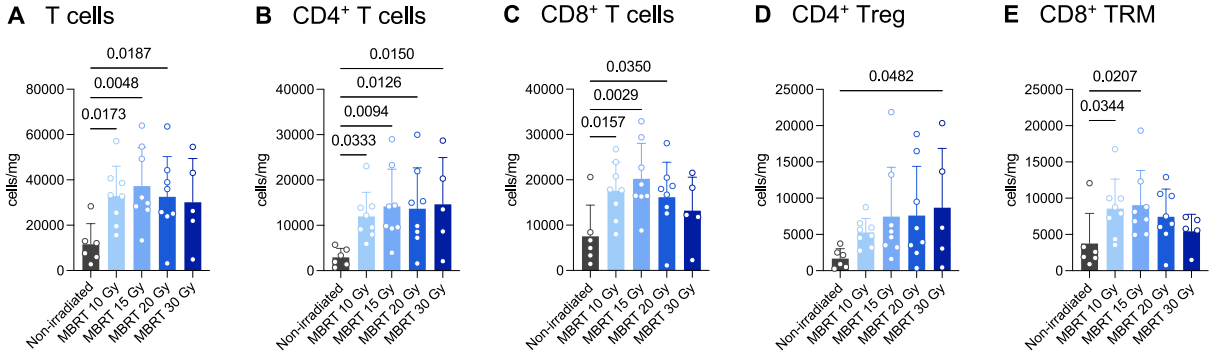

Fig. 4. Dose heterogeneity controls tumor infiltration. FACS analysis of immune cells in glioblastoma 7 days after X-ray MBRT treatment in a dose escalation. (A) Cell density including all T cells ($CD3^+$), (B) $CD4^+$ T cells, (C) $CD8^+$ T cells, (D) regulatory T cells ($CD4^+$ Tregs), (E) tissue resident memory ($CD8^+$ TRM) T cells. The data are presented as the mean ± standard deviation (SD).

valley doses at the tumor without the need of extremely high mean and peak doses; ii) the use of protons results in more conformal dose distributions, with less dose deposited in normal tissues; iii) there are indications that protons lead to distinct radiobiology, including a potential more effective immune priming, which might result in relevant synergies with MBRT.

Recent studies revealed an important role of the immune system in the anti-tumor response of MBRT, and SFRT in general, with T cells playing a major role [23,24,32]. The exact mechanisms and influence of peak and valley doses are still elusive. It has been hypothesized that the immunomodulatory effects in SFRT could be linked to the deposited peak dose, which triggers the release of tumor neoantigens by inducing tumor cell death [33]. However, low radiation doses can reprogram an immunosuppressive TME to a more immunogenic one, and thus valley doses could also play an important role [34,35]. RG2 cells represent a highly invasive and low immunogenic rat glioblastoma model, similar in a sense to human glioblastomas, with highly immunosuppressive TME, so this model aligns seamlessly with our research interest. One aim of this study is to shed some light in that direction.

Our results confirmed that link between valley dose and ILS found in a previous retrospective evaluation [26], while also leading to a globally similar immune infiltration. In contrast, the level of dose heterogeneity or spatial fractionation, and thus the PVDR (driven by peak dose), differed among groups and appeared to influence the number of long-term survivors free of tumor (tumor eradication) and modulate the density of Tregs and $CD43^{+}$ monocytes. Higher dose heterogeneity (higher PVDR and peak dose) results in a less immunosuppressive TME, which might explain the higher number of long-term survivals. Indeed, the vestige of a strong immune infiltration (T cells and macrophages) located in the pre-existing tumor bed was observed 3 months after irradiation in this case (2.8 mm c-t-c) and could indicate an active immune monitoring, thus allowing long-term antitumor immunity [24]. However, no comparative study with uniform dose deposition (CPT) was conducted in the long-term survival study, as a minimum dose of 10 Gy CPT is not sufficient to achieve tumor eradication in this glioblastoma model (13).

The influence of the dose heterogeneity on immunomodulation was also supported by the comparison with CPT (homogenous) irradiations, which showed a higher cell density of neutrophils, $CD43^{+}$ monocytes and $CD49d^{neg}$ macrophages likely related to acute inflammatory signals, in comparison with the pMBRT group. This suggests a more immunosuppressive function in the TME after CPT than in pMBRT and highlights the potential impact of dose homogenization on promoting immunosuppression. Our unpublished data [36] shows that the density of Treg in RG2-glioma bearing rats after 25 Gy delivered conventionally in one fraction is similar in number to the Treg density after irradiation with the 2.0 mm c-t-c collimator.

To decorrelate the influence of the dose heterogeneity (PVDR) and peak dose, an additional experiment was carried out. One of the limitations of the study is that, due to restricted access to the proton therapy center, the dose escalation study had to be performed using X-ray MBRT. The change of radiation type for this first study does not influence the conclusions. Furthermore, no direct comparison between protons and X-rays was intended. This time, dose heterogeneity was kept constant, the valley dose varies only slightly, while peak and mean doses varied significantly. Interestingly, T cells infiltration was similar in all the groups, and that, even with very high peak doses (84 Gy) used and were similar to what we have obtained in pMBRT configurations. This suggests that the nature of the dose distribution heterogeneity, rather than the mean, peak or valley dose, may play a crucial role in shaping a favorable immune composition.

Yet, one could argue that the c-t-c distance (2.8 mm c-t-c versus 2.0 mm c-t-c) might play a major role. However, it should be noted that in the latter dose escalation study, the PVDR (PVDR = 18) was significantly higher than in the pMBRT study (PVDR = 5 and 3, respectively). Additionally, the c-t-c distance was kept constant and narrower than in the first study (1.4 mm here versus 2.8 or 2.0 mm in the pMBRT comparative study). Moreover, the ratio of volume receiving peak doses with respect to c-t-c was similar between the MBRT dose escalation study (around 50 %) and the pMBRT 2.0 mm c-t-c irradiations (with a 1 mm beam width in the rat head, thus 50 %). However, in the MBRT dose escalation study, no significant increase of Tregs is observed contrary to the 2.0 mm c-t-c pMBRT irradiations.

All the aforementioned observations suggest that the dose gradients are key players in reducing immunosuppression. One potential explanation is that they might allow to exploit all the different radiation immunomodulatory regimes: TME-modulation at low doses, immune-modulation at sub-ablative doses and immunogenic cell death at ablative doses [37].

The observations of the present work could also explain the superior tumor control and proportion of long-term survivors free of tumor (67 %) without brain lesions obtained in glioma-bearing rats irradiated with pMBRT in a previous work, with a dose heterogeneity of 1.2 in the target as compared with the group which received CPT homogenous dose distributions (22 % long-term survivors free of tumor) [4].

The reduced immunosuppression when spatial fractionation (dose heterogeneity) is employed might also explain why SFRT appears to be more effective than conventional RT in radio-immunotherapy combinations [33].

Conclusions

This work emphasizes the importance of dose heterogeneity (quantified by the PVDR) in pMBRT and its immunomodulatory capacity. Our findings demonstrate that dose heterogeneity lowers tumor immunosuppression while improving long-term survival. Therefore, and contradicting the classical paradigm of radiation therapy, dose heterogeneity in the tumor, respecting a minimum valley dose [26], is advisable. This could also enhance the outcome of radio-immunotherapy combinations.

Our study paves the way for further optimization of pMBRT and its therapeutic application, particularly for radioresistant tumors, such as glioblastomas.

Research data are stored in an institutional repository and will be shared upon request to the corresponding author.

Funding statement

This project received funding from the European Research Council (ERC) under the European Union's Horizon 2020 research and innovation program (Grant Agreement No 817908).

Calculation time was granted at the supercomputer Joliot Curie SKL (Irene_skylake), Très Grand Centre de Calcul (TGCC) of Commissariat d'Energie Atomique (CEA), from the Partnership for Advanced Computing in Europe (PRACE Project Access Call 21rst, proposal number 2020225339).

Declaration of competing interest

The authors declare that they have no known competing financial interests or personal relationships that could have appeared to influence the work reported in this paper.

Acknowledgements

This project received funding from the European Research Council (ERC) under the European Union's Horizon 2020 research and innovation program (Grant Agreement No 817908). The authors warmly thank Charlène Lasgi (Cytometry Platform, CurieCoretech, Institut Curie, 91400 Orsay, France) and the Institut Curie cytometry platform for the support in flow cytometry experiments. The authors thank the experimental radiotherapy platform (Radexp) at Institut Curie, for support in the irradiations and tumor implantations. The authors greatly thank Cédric Messaoudi for his time and expertise on image analysis and greatly acknowledge the Multimodal Imaging Center Imaging Facility of Institut Curie (CNRS UMS2016/ Inserm US43/ Institut Curie / Université Paris-Saclay). The authors thank Sophie Leboucher (Histology platform, CurieCoreTech, Institut Curie, 91400 Orsay, France) at the

Institut Curie histology platform for the equipment supplied. This work has benefited from the facilities and expertise of Cell and Tissue Imaging Platform at Institut des Neurosciences de Paris-Saclay (NeuroPsi, CEA Campus, 91400 Saclay, France).

Appendix A. Supplementary data

Supplementary data to this article can be found online at https://doi.org/10.1016/j.radonc.2024.110577.

References

[1] Prezado Y, Fois GR. Proton-minibeam radiation therapy: a proof of concept. Med Phys 2013 Mar;40:031712.
[2] Prezado Y. Proton minibeam radiation therapy: a promising therapeutic approach for radioresistant tumors. C R Biol 2021 Dec 20;344:409–20.
[3] Prezado Y, Jouvion G, Patriarca A, Nauraye C, Guardiola C, Juchaux M, et al. Proton minibeam radiation therapy widens the therapeutic index for high-grade gliomas. Sci Rep 2018 Nov 7;8:16479.
[4] Prezado Y, Jouvion G, Guardiola C, Gonzalez W, Juchaux M, Bergs J, et al. Tumor Control in RG2 Glioma-Bearing Rats: A Comparison Between Proton Minibeam Therapy and Standard Proton Therapy. Int J Radiat Oncol Biol Phys 2019 Jun 1;104:266–71.
[5] Lamirault C, Brisebard E, Patriarca A, Juchaux M, Crepin D, Labiod D, et al. Spatially Modulated Proton Minibeams Results in the Same Increase of Lifespan as a Uniform Target Dose Coverage in F98-Glioma-Bearing Rats. Radiat Res 2020 Dec 1;194:715–23.
[6] Bertho A, Ortiz R, Juchaux M, Gilbert C, Lamirault C, Pouzoulet F, et al. First Evaluation of Temporal and Spatial Fractionation in Proton Minibeam Radiation Therapy of Glioma-Bearing Rats. Cancers 2021 Sep 28;13:4865.
[7] Prezado Y, Jouvion G, Hardy D, Patriarca A, Nauraye C, Bergs J, et al. Proton minibeam radiation therapy spares normal rat brain: Long-Term Clinical, Radiological and Histopathological Analysis. Sci Rep 2017 Oct 31;7:14403.
[8] Lamirault C, Doyère V, Juchaux M, Pouzoulet F, Labiod D, Dendale R, et al. Short and long-term evaluation of the impact of proton minibeam radiation therapy on motor, emotional and cognitive functions. Sci Rep 2020 Aug 11;10:13511.
[9] Sammer M, Teiluf K, Girst S, Greubel C, Reindl J, Ilicic K, et al. Beam size limit for pencil minibeam radiotherapy determined from side effects in an in-vivo mouse ear model. PLoS One 2019;14:e0221454.
[10] Girst S, Greubel C, Reindl J, Siebenwirth C, Zlobinskaya O, Walsh DWM, et al. Proton Minibeam Radiation Therapy Reduces Side Effects in an In Vivo Mouse Ear Model. Int J Radiat Oncol Biol Phys 2016 May 1;95:234–41.
[11] Kundapur V, Mayer M, Auer RN, Alexander A, Weibe S, Pushie MJ, et al. Is Mini Beam Ready for Human Trials? Results of Randomized Study of Treating De-Novo Brain Tumors in Canines Using Linear Accelerator Generated Mini Beams. Radiat Res 2022 Aug 1;198:162–71.
[12] Prezado Y. Divide and conquer: spatially fractionated radiation therapy. Expert Rev Mol Med 2022;24:e3.
[13] Bouchet A, Serduc R, Laissue JA, Djonov V. Effects of microbeam radiation therapy on normal and tumoral blood vessels. Phys Med 2015 Sep;31:634–41.
[14] Bouchet A, Lemasson B, Le Duc G, Maisin C, Bräuer-Krisch E, Siegbahn EA, et al. Preferential Effect of Synchrotron Microbeam Radiation Therapy on Intracerebral 9L Gliosarcoma Vascular Networks. International Journal of Radiation Oncology*Biology*Physics 2010 Dec;78:1503–12.
[15] Sabatasso S, Laissue JA, Hlushchuk R, Graber W, Bravin A, Bräuer-Krisch E, et al. Microbeam radiation-induced tissue damage depends on the stage of vascular maturation. Int J Radiat Oncol Biol Phys 2011 Aug 1;80:1522–32.
[16] Bertho A, Ortiz R, Maurin M, Juchaux M, Gilbert C, Espenon J, et al. Thoracic Proton Minibeam Radiation Therapy: Tissue Preservation and Survival Advantage Over Conventional Proton Therapy. International Journal of Radiation Oncology*Biology*Physics 2024. S0360301624005108.
[17] Asur RS, Sharma S, Chang CW, Penagaricano J, Kommuru IM, Moros EG, et al. Spatially fractionated radiation induces cytotoxicity and changes in gene expression in bystander and radiation adjacent murine carcinoma cells. Radiat Res 2012 Jun;177:751–65.
[18] Asur R, Butterworth KT, Penagaricano JA, Prise KM, Griffin RJ. High dose bystander effects in spatially fractionated radiation therapy. Cancer Lett 2015 Jan;356:52–7.
[19] Dilmanian FA, Button TM, Le Duc G, Zhong N, Peña LA, Smith JAL, et al. Response of rat intracranial 9L gliosarcoma to microbeam radiation therapy. Neuro Oncol 2002 Jan;4:26–38.
[20] Dal Bello R, Becher T, Fuss MC, Krämer M, Seco J. Proposal of a Chemical Mechanism for Mini-Beam and Micro-Beam Efficacy. Front Phys 2020 Oct;22:564836.
[21] Bouchet A, Lemasson B, Christen T, Potez M, Rome C, Coquery N, et al. Synchrotron microbeam radiation therapy induces hypoxia in intracerebral gliosarcoma but not in the normal brain. Radiother Oncol 2013 Jul;108:143–8.
[22] Potez M, Fernandez-Palomo C, Bouchet A, Trappetti V, Donzelli M, Krisch M, et al. Synchrotron Microbeam Radiation Therapy as a New Approach for the Treatment of Radioresistant Melanoma: Potential Underlying Mechanisms. Int J Radiat Oncol Biol Phys 2019 Dec 1;105:1126–36.
[23] Bazyar S, O'Brien ET, Benefield T, Roberts VR, Kumar RJ, Gupta GP, et al. Immune-Mediated Effects of Microplanar Radiotherapy with a Small Animal Irradiator. Cancers (Basel) 2021 Dec 29;14:155.
[24] Bertho A, Iturri L, Brisebard E, Juchaux M, Gilbert C, Ortiz R, et al. Evaluation of the Role of the Immune System Response After Minibeam Radiation Therapy. Int J Radiat Oncol Biol Phys 2022 Aug 17;S0360–3016:03106.
[25] Prezado Y, Grams M, Jouglar E, Martínez-Rovira I, Ortiz R, Seco J, et al. Spatially fractionated radiation therapy: a critical review on current status of clinical and preclinical studies and knowledge gaps. Phys Med Biol 2024. May 21;69(10):10TR02.
[26] Fernandez-Palomo C, Chang S, Prezado Y. Should Peak Dose Be Used to Prescribe Spatially Fractionated Radiation Therapy?-A Review of Preclinical Studies. Cancers (Basel) 2022 Jul 26;14:3625.
[27] Mayr NA, Snider JW, Regine WF, Mohiuddin M, Hippe DS, Peñagarícano J, et al. An International Consensus on the Design of Prospective Clinical-Translational Trials in Spatially Fractionated Radiation Therapy. Adv Radiat Oncol 2022;7:100866.
[28] Barth RF. Rat brain tumor models in experimental neuro-oncology: the 9L, C6, T9, F98, RG2 (D74), RT-2 and CNS-1 gliomas. J Neurooncol 1998 Jan;36:91–102.
[29] De Marzi L, Patriarca A, Nauraye C, Hierso E, Dendale R, Guardiola C, et al. Implementation of planar proton minibeam radiation therapy using a pencil beam scanning system: A proof of concept study. Med Phys 2018 Nov;45:5305–16.
[30] Ortiz R, De Marzi L, Prezado Y. Preclinical dosimetry in proton minibeam radiation therapy: Robustness analysis and guidelines. Med Phys 2022 Aug;49:5551–61.
[31] Messaoudi C. Multimodal Imaging Center, Institut Curie. GitHub - Multimodal Imaging Center/MIC-MAQ for Microscopy Images of Cells -. Available from: Multi Analyses and Quantifications [Internet] 2023. https://github.com/MultimodalImagingCenter/MIC-MAQ.
[32] Kanagavelu S, Gupta S, Wu X, Philip S, Wattenberg MM, Hodge JW, et al. In vivo effects of lattice radiation therapy on local and distant lung cancer: potential role of immunomodulation. Radiat Res 2014 Aug;182:149–62.
[33] Jiang L, Li X, Zhang J, Li W, Dong F, Chen C, et al. Combined High-Dose LATTICE Radiation Therapy and Immune Checkpoint Blockade for Advanced Bulky Tumors: The Concept and a Case Report. Front Oncol 2020;10:548132.
[34] Herrera FG, Ronet C, Ochoa de Olza M, Barras D, Crespo I, Andreatta M, et al. Low-Dose Radiotherapy Reverses Tumor Immune Desertification and Resistance to Immunotherapy. Cancer Discov 2022 Jan;12:108–33.
[35] Klug F, Prakash H, Huber PE, Seibel T, Bender N, Halama N, et al. Low-dose irradiation programs macrophage differentiation to an iNOS^{+}/M1 phenotype that orchestrates effective T cell immunotherapy. Cancer Cell 2013 Nov 11;24:589–602.
[36] Iturri, Lorea, Juchaux, Marjorie, Gilbert, Cristèle, Espenon, Julie, Prezado, Yolanda. On the Optimal Fractionation Scheme for Lymphocyte Infiltration in Glioblastoma Radiotherapy Treatment. Unpublished results.
[37] Demaria S, Guha C, Schoenfeld J, Morris Z, Monjazeb A, Sikora A, et al. Radiation dose and fraction in immunotherapy: one-size regimen does not fit all settings, so how does one choose? J Immunother Cancer 2021 Apr;9:e002038.